Automatic Localization and Characterization of Mid-latitude Ionospheric Plasma Structures from All-sky Airglow Images using Deep Learning Framework

Satarupa Chakrabarti[1,2], Jeevan Upadhyaya[1], Rahul Rathi[1,3], Virendra Yadav[4], Dipjyoti Patgiri[1], Gaurav Dixit[5], M.V. Sunil Krishna[1,6], Sumanta Sarkhel[1,6,*]

[*]Sumanta Sarkhel, Department of Physics, Indian Institute of Technology Roorkee, Roorkee - 247667, Uttarakhand, India (sarkhel@ph.iitr.ac.in)

[1]Department of Physics, Indian Institute of Technology Roorkee, Roorkee – 247667, Uttarakhand, India

[2]School of Electrical Engineering and Computer Science, KTH Royal Institute of Technology, 114 28 Stockholm, Sweden

[3]Physics Department, Lancaster University, Lancaster, United Kingdom

[4]Aryabhatta Research Institute of Observational Sciences, Nainital – 263001, Uttarakhand, India

[5]Department of Management Studies, Indian Institute of Technology Roorkee, Roorkee – 247667, Uttarakhand, India

[6]Centre for Space Science and Technology, Indian Institute of Technology Roorkee, Roorkee –247667, Uttarakhand, India

Email Addresses: chakrabartisatarupa@gmail.com (Satarupa Chakrabarti), jeevan_u@ph.iitr.ac.in (Jeevan Upadhyaya), rrathi@ph.iitr.ac.in (Rahul Rathi), virendra@aries.res.in (Virendra Yadav), dipjyoti_p@ph.iitr.ac.in (Dipjyoti Patgiri), gaurav.dixit@ms.iitr.ac.in (Gaurav Dixit), mv.sunilkrishna@ph.iitr.ac.in (M. V. Sunil Krishna), sarkhel@ph.iitr.ac.in (Sumanta Sarkhel)

Abstract

This paper brings forth a new automatic approach to determine the propagation parameters (horizontal velocity, propagation direction, and orientation) of mid-latitude ionospheric plasma structures (MIPS) using airglow images recorded by an all-sky airglow imager located at Hanle, Ladakh, India. The proposed approach is an amalgamation of two frameworks – a hybrid deep learning image segmentation model for localization along with automatic determination of parameters using the intensity minima of the MIPS. Designed in the form of a pipeline, the frameworks are executed sequentially. The propagation parameters obtained from the automatic method have been compared with the results of a previously implemented semi-automatic approach. Comparison between the two approaches revolves around the error involved, time complexity, and dependency on the morphology of the plasma structures. The results suggest that the proposed method can be adopted over the semi-automatic approach as it has less error, minimal dependency on the morphology of the structures, and less time-exhaustive.

Keywords: All-sky airglow imager; Image segmentation; Mid-latitude ionospheric plasma structure; Deep learning.

Highlights:

- A new automatic method is developed to localize and determine the propagation parameters of MIPS.
- The proposed method performed better when results were compared with a semi-automatic approach.
- The automatic approach has less error, low time complexity, and minimum dependency on the morphology of plasma structures.

1. Introduction

The mid-latitude ionosphere was historically considered quiescent in nature. However, with the advancement of different probing techniques (ionosonde, incoherent scatter radar, airglow photometers and imagers) it is observed that different ionospheric plasma structures (irregularities) occur even in the mid-latitude region (Benzcze & Bakki, 2002; Bowman, 1981; Figueiredo et al., 2018; Fukao et al., 1991; Huang et al., 2018; Mathews et al., 2001; Miller, 1997; Otsuka et al., 2004, 2008; Shiokawa et al., 2008; Sivakandan et al., 2020, 2021; Sun et al., 2015). These plasma structures include medium scale traveling ionospheric disturbances (MSTIDs) and mid-latitude field-aligned plasma depletion (MFPD). MSTIDs are propagating low and high electron density structures in the mid-latitude ionosphere having a preferential orientation of the fronts in both hemispheres (Ding et al., 2011; Hocke and Schlegel, 1996; Huang et al., 2016, 2018; Otsuka et al., 2004; Shiokawa et al., 2003a, 2005; Sun et al., 2015). Whereas, MFPDs are geomagnetically field-aligned plasma structures which cause the appearance of spread-F in ionograms (Fukao et al., 1988; Sivakandan et al, 2020; Yadav et al., 2021a; and references therein). Previous studies have revealed that the propagative characteristics (velocity and orientation) of the mid-latitude ionospheric plasma structures (MIPS) play a crucial role in their dynamics (Otsuka et al., 2012; Patgiri et al., 2024a; Rathi et al., 2022, 2024; Wu et al., 2021; Yadav et al., 2021a). These studies reported that due to the change in orientation and/or velocity resulted in interaction, merging, distortion, and dissipation of these structures. Therefore, precise determination of these propagative characteristics is essential in studying the different phenomena associated with these structures.

In recent years, quite a few methods have been developed and implemented to estimate these characteristics. A semi-automatic approach was developed and used by Yadav et al. (2021a) to investigate multiple fronts of an MSTID. Furthermore, the same method was applied to study various MSTID events involving interaction, merging, and dissipation (Patgiri et al., 2024a; Rathi et al., 2021, 2022; Yadav et al., 2021b). A 3-D spectral analysis method was also applied to all-sky airglow images to determine the horizontal velocity, propagation direction and period (Takeo et al., 2017; Tsuboi et al., 2023). In another recent study, Liu et al. (2022) determined various characteristics of MSTIDs using TEC maps. These studies have determined different parameters, however, they were unable to provide any information about the velocity of the individual bands of MSTIDs and find their respective orientation. At present, finding propagation parameters of plasma structures is primarily based on semi-automatic approaches that require manual intervention thus making it difficult, time-consuming, and subject to human error when the dataset is large-scale and spanning over years.

The advent of deep learning algorithms has transformed the analysis of large datasets by bringing forth approaches that are capable of feature extraction, transformation, segmentation, and classification. With the amalgamation of deep learning techniques in the domain of space sciences, researchers have applied a variety of techniques for image segmentation in studying the complex and dynamic patterns of auroral images (Gao et al., 2011; Niu et al., 2018), cloud classification (Fabel et al., 2022; Hasenbalg et al., 2020; Xie et al., 2020; Zhang et al., 2018), gravity wave identification (Kumar et al., 2023; Lai et al., 2019) and so on. Previous studies on airglow images have mostly focused on understanding the generation mechanism of plasma irregularities, finding statistical characteristics (Lai et al., 2023), and analysis of these structures through image classification using conventional as well as machine learning approaches (Chakrabarti et al., 2024a; Githio et al., 2024). Therefore, the localization of MIPS and determination of their characteristics with the help of a deep learning approach is a first of its kind in this domain.

In this study, we present a hybrid deep learning algorithm for all-sky airglow image segmentation to localize MIPS. A major contribution of this work is the custom-designed framework that is capable of finding the propagation parameters of these structures without any manual intervention. The paper is structured as follows. The two frameworks and their workings are introduced in section 2 along with the dataset description. Section 3 describes the detailed evaluation and discussion of experimental outcomes, followed by the conclusion in section 4.

2. Data and Frameworks

2.1 Data Description

The dataset used in the present study is from a multi-wavelength all-sky airglow imager installed at Hanle (32.77°N, 78.97°E), Ladakh, India, that captures raw images of two airglow emissions (557.7 nm and 630.0 nm). The raw images are then processed for geospatial calibration where the corresponding latitude and longitude value of each pixel is calculated. This is followed by noise removal and unwarping of images to get the final processed images. A detailed description of the image processing techniques is given by Mondal et al. (2019). In the present study, we have used 630.0 nm unwarped airglow images (spanning over the latitude and longitude of 28 – 39°N and 73 – 86°E, respectively; as presented in Figure 1) for the localization and characterization of MIPS using a combined approach of deep learning segmentation and automatic parameterization. The hybrid deep learning model for image segmentation is trained using nearly 1700 unwarped images consisting of single as well as multiple band plasma structures and their respective ground truth (a binary image/mask that serves as the reference for evaluating the image segmentation algorithm by highlighting the structures as zero/black and background as one/white) that spanned over five years (from 2018 to 2022). It is to be noted that most of the events (~ 96%) during these five years occurred during geomagnetically quiet time. The images of these events used as input in the hybrid deep learning model were previously classified as 'presence of plasma structures' by a separate, stand-alone convolutional neural network model (Chakrabarti et al., 2024a). To the best of our knowledge, studies pertaining to the automatic characterization of MIPS were not reported in the literature. Therefore, we developed an automatic approach to find the propagation parameters of these structures. As mentioned previously, MIPS can appear as single or multiple bands in the all-sky airglow images but the present work revolves around only single dark band plasma structures. Five such events of single dark band structures with different morphologies (shape and size) were considered.

2.2 Proposed Methodology

The proposed methodology has two separate frameworks – the first framework chiefly consists of two steps, as shown in Figure 2, for image segmentation using a deep learning approach. The second framework, as presented in Figure 4, is a combination of multiple steps for finding the propagation parameters automatically. Detailed descriptions of the proposed frameworks are mentioned below.

Framework 1: Deep learning-based image segmentation

Step 1: Pixel thresholding for generation of mask

Thresholding is an approach to convert a gray-scaled image to a binary image or 'mask' such that the objects present in the image can be separated from the background (Bovik, 2009). The pixels are defined on their intensity value and are generally denoted as either 0 or 1 based on a particular threshold value. A binary mask is generated where it defines the region of interest (ROI). The ROI and background are defined by either 0 or 1 (Bovik, 2009). In this work, single thresholding was performed, where the intensity is above or below a specified threshold. The single pixel thresholding approach has three main functions – histogram stretch, mapping of intensity level and finally the thresholding. The histogram stretch function uses minimum and maximum intensity values on the image, followed by mapping each intensity level to an output intensity level. The final function is thresholding, where a desired threshold value is given to generate the masked image that serves as the ground truth in the image segmentation model.

Step 2: Hybrid image segmentation model

The architecture of the image segmentation model is based on the combination of the VGG16 and the U-Net model (Ronneberger et al., 2015). Leveraging the pre-trained feature extraction competency of VGG16 while exploiting the unique U-shaped symmetrical architecture of the encoder-decoder (Shelhamer et al., 2017) with skip connections in between makes this framework robust and efficient for image segmentation. The convolutional layers of VGG16 (Ayeni, 2022; Simonyan & Zisserman, 2014) are capable of extracting rich features from the input images and comprise the top half of the hybrid model, which is used as an encoder or the down-sampling path. The decoder of the U-Net, also known as the up-sampling path, uses transposed convolutions (deconvolution) for the reconstruction of the spatial dimension of the image (Fabel et al., 2022). The skip connections play a crucial role in integrating and retaining the fine-grained details of the encoder layer to the decoder layer during the up-sampling process (Wang et al., 2022). These connections are responsible for the concatenation of output from a preceding layer with the batch-normalized output of the corresponding encoder layer (Ioffe & Szegedy, 2015). The presence of skip connections enables feature channels in the decoder to encompass contextual information that aids in explicit localization (Fabel et al., 2022). The overview of the entire image segmentation framework is presented in Figure 2. The deep learning model used Adam optimizer (learning rate of 0.0001) and standard binary cross-entropy as the loss function with the rest of the default parameters. This hybrid model entailed robust feature extraction and detailed localization which made it suitable for the image segmentation task. Figure 3 shows five instances of single-band MIPS that were segmented using the aforementioned hybrid approach. The figure depicts the original unwarped images, their masked counterparts that served as the ground truth and the obtained segmented images from the deep learning model. The algorithm of Framework 1 is mentioned in Appendix A along with the working principle of the hybrid image segmentation model.

Framework 2: Automatic estimation of propagation parameters (Velocity, propagation direction, and tilt angle)

Step 1: Loading segmentation model and input file

The trained hybrid deep learning model was used to localize single dark band MIPS from the unwarped input file and generate the corresponding segmented images.

Step 2: Locating the MIPS and condition to skip frames

The segmented images generated by Framework 1 were subjected to row-wise scanning to find the intensity minima of the structure and their pixel coordinates (x, y) as shown in Figure 4(a & b). The obtained coordinates of the minima points were used to plot a best-fit line (least-square fit method) in each of the frames. While plotting the best-fit line, it was observed that a few outlier points were degrading the line fitting. In order to reduce the number of such outlier points, a condition was applied that automatically removed the points which have higher squared error than the average squared error of all the points from the initial best-fit line. Two examples are shown for pictographic explanation of the approach involved in plotting the first and the second best-fit line. The white dots in all the sub figures of Figure 5 represent the minima points obtained after row scanning, which are then used to draw the best fit line as marked in red. Outlier minima points (few instances shown as dashed circle in Figure 5a) having higher squared error than the average squared error is removed before plotting the second best-fit line. The scenario after removal of these outliers is presented in Figure 5b where locations of previously present outlier minima points are marked in dashed circle along with the second best-fit line. These second best-fit lines were used to calculate the propagation velocity as shown in Figure 4c – e. However, it is evident from the segmented images (Figure 3), that single dark band MIPS vary in morphology with some having sharp and defined structures, while others having diffused structures. As expected, the diffused and distorted structures (Figure 3d–e) tend to have more scattered minima points that can lead to an overlap of points in the successive frames, which may affect the velocity calculation. To address such scenarios, instead of successive frames, a skipping condition is incorporated in the algorithm that processes alternate frames (one skip). For the skipping condition, the average squared error of all the minima points from the second best-fit line is calculated. The framework skips the frames if the number of such minima points fail to cross seventy-five percent (a substantial coverage of minima points) of the total minima points while lying within the average squared error value.

Step 3: Determination of propagation parameters and error calculation

After the skip condition, the velocity was calculated using the perpendicular distance between the best-fit lines of the two frames (including events where a skip was required) as shown in Figure 4e. The perpendicular distance was calculated from the mid-point of the best-fit line of one frame to that of the next one using the corresponding zonal and meridional distance coordinates. The algorithm of Framework 2 is mentioned in Appendix B. The framework also determines the propagation direction and orientation of the MIPS (anti-clockwise from geomagnetic north-south) using the slope of the second best-fit line. Since this approach is based on the concept of best-fit line, it will have an error when the parameters are determined. Therefore, this framework also estimates the error involved while calculating the velocity, propagation direction, and tilt angle. The schematic representation of the methods used to calculate the error involved in determination of velocity, propagation direction, and tilt angle are presented in Figure 6. Figure 6a shows the second best-fit lines that has been used to calculate the velocity of the ionospheric plasma structures. Figure 6b presents the approach to determine the error involved in plotting of the best-fit lines. To estimate this error, the method of standard error (SE) is used to find the margin between which the best-fit lines can lie depending on the spread of the minima points. Here, Δd is the distance error in plotting the best-fit line. Therefore, in determining the velocity error between two frames we have considered the distance error of each frame (Δd_1, Δd_2, …Δd_n, where n = number of frames). Based on this the total error in velocity between two frames is calculated as $(\Delta d_1 + \Delta d_2)/\Delta t$, where Δt is the time difference between two frames. Figure 6c shows the approach to calculate the tilt angle (θ) and propagation direction ($\phi = \theta + 90^{\circ}$) from the geomagnetic north-south (anti-clockwise). Figure 6d is the schematic representation of the approach to determine the error involved in calculating the propagation direction and tilt angle. The dashed lines represent the error margins as shown in Figure 6b. Errors can be approximated by how much the slope of the best-fit line can vary within the error margins. The error lies between the best-fit line and the line (passing through the midpoint of the best-fit line) connecting the two endpoints of the error margins.

3. Results and Discussion

Mid-latitude ionospheric plasma structures are often observed as a single dark band (MFPD) as well as multiple (bright and dark) bands (MSTIDs) (Figueiredo et al., 2018; Paulino et al., 2018; Pimenta et al., 2008; Rathi et al., 2021; Sivakandan et al., 2020). Recently, a few studies have reported interaction between these plasma structures which led to certain post-interaction phenomena such as – merging, bifurcation, and dissipation (Wu et al., 2021, Patgiri et al., 2024a; Rathi et al., 2021, 2022; Yadav et al., 2021b). They have enumerated various factors – horizontal velocity, orientation, propagation direction, and polarization electric field of these plasma structures that play a crucial role in their interactions. Therefore, the accurate determination of their horizontal velocity, propagation direction, and orientation (tilt angle) is necessary to comprehensively understand the phenomena associated with these MIPS.

As previously mentioned, various authors have developed and applied different approaches to determine the propagative characteristics of the MIPS. Yadav et al. (2021a), developed a semi-automatic approach to find the horizontal velocity and orientation of MSTID bands observed in the 630.0 nm airglow images. The method requires visual inspection of the MSTID bands to manually locate and mark two points along a straight part of the front's edge. Using the coordinates of the two points, a straight line is drawn. This step is repeated for all the images of any particular event. With the help of such lines in successive images, the method determines the horizontal velocity and tilt angle of the MSTID bands. Although this method was used in multiple studies (Patgiri et al., 2024a, 2024b; Rathi et al., 2021, 2022; Yadav et al., 2021b), there are certain major drawbacks associated with it. As this method involves manual intervention, there is a high degree of subjectivity and human error. This error can be reduced to an extent with the repetition of steps over multiple iterations which is quite time-consuming. Also, this approach only works for MSTID bands having distinct and straight edges and fails when the edges are distorted or diffused. Due to these shortcomings of the semi-automatic approach, the present study puts forth an automatic method which requires no human intervention, is less time-consuming, and can work on any type (diffused/distorted) of mid-latitude plasma structures.

The automatic method encompassed two frameworks – a deep learning-based image segmentation for localizing the MIPS (refer subsection 2.2, Framework 1) and an automatic estimation of propagation parameters (refer subsection 2.2, Framework 2). Framework 2 in its current form is capable of determining the propagation parameters of MIPS consisting of only a single dark band. More than six years of data were meticulously checked and five events exhibiting single dark band MIPS were identified. Following the localization of the structures in the airglow images, the automatic approach was applied to these five events. Figure 7 presents a comparative overview of the results obtained when both, the proposed automatic approach (blue curve) as well as the semi-automatic approach (red curve), were applied to the five events. The top panels (Figures 7a – e) show the temporal variation of the horizontal velocity, the middle panels (Figures 7f – j) present the tilt angle (orientation), and the bottom panels (Figures 7k – o) represents the propagation direction from the geomagnetic N-S (anti-clockwise). Temporal average of the parameters (horizontal velocity with zonal and meridional component, tilt angle, and propagation direction) for each event with their respective error involved is presented in Tables 1 & 2.

For the first three events (9 October 2018, 29 October 2018, and 16 January 2021), the trend in the temporal variation of the horizontal velocity, tilt angle, and propagation direction of the structures are nearly similar (Figures 7a–c, f–h, & k–m) while in the remaining two events (11 August 2021 and 2 July 2022) the values obtained from the two methods differ considerably (Figures 7d–e, i–j, & n–o). The reason behind this significant difference lies in their morphology. As mentioned earlier, the semi-automatic approach only works for structures having clear and straight edges. Therefore, whenever it encounters diffused or distorted structures (the last two events as shown in Figures 3d–e, i–j & n–o), only a small portion of the structure having a straight edge is considered. Hence, the values obtained may not represent the entire structure and will have larger errors as evident from Figures 7d–e, i–j, & n–o. Thus, in such scenarios, the semi-automatic method fails to accurately determine the propagation parameters. Apart from the dependency on morphology, the semi-automatic approach involves manual intervention which leads to subjectivity and additional human error that again gets reflected in the obtained parameters. This is evident from the larger error values in Tables 1 & 2. On the other hand, as the proposed automatic approach considers the intensity minima of the entire structure, the morphology of the structure has minimal impact in determining the parameters. Hence, it overcomes the major shortcomings of the semi-automatic method. Since it is devoid of any manual interference, it also reduces the chance of any additional error (refer to Tables 1 & 2).

The proposed automatic method is less exhaustive with low time complexity and involves less error, which makes it a favorable alternative over the semi-automatic approach and suitable for analyzing large amounts of data for any future statistical studies. However, the only limitation of the automatic approach is that it is only capable of determining the propagation parameters of single dark band MIPS at present. As mentioned earlier, these MIPS can have multiple bands which enhances the complexity in determining the propagation parameters of every front at the same time. Thus, the future scope of this work lies in extending and upgrading this approach for events having multiple bands.

4. Conclusion

The present study utilizes a hybrid deep learning algorithm for the localization of mid-latitude ionospheric plasma structures through image segmentation and introduces a new automatic approach for the determination of propagation parameters (horizontal velocity, propagation direction, and tilt angle) using all-sky airglow images. This work comprises two frameworks that are connected in a pipeline. The first framework is responsible for localizing the plasma structures from airglow images using a hybrid deep learning model of VGG16 – U-Net. The output (segmented images) of this framework is used in the second framework which uses the minimum intensity of the plasma structures to automatically estimate the propagation parameters. The proposed method was applied to five separate events of single dark band plasma structures and the values of the estimated parameters were compared to a previously used semi-automatic approach. The results suggest that the automatic method performs better with respect to the error involved, time complexity and dependency on the morphology of the plasma structures. However, in the present form, the proposed method is only capable of determining the characteristics of single dark band plasma structures. Addressing multiple bands and finding their propagation parameters is complex and challenging, which is the future scope of the present study.

Data availability

The input image, ground truth and the model segmented output images are publicly available at Chakrabarti et al. (2024b).

Acknowledgements

S. Sarkhel acknowledges the financial support from the Anusandhan National Research Foundation, Government of India (CRG/2021/002052) to maintain the multi-wavelength airglow imager. The support from the Indian Astronomical Observatory (operated by the Indian Institute of Astrophysics, Bengaluru, India), Hanle, Ladakh, India, for the day-to-day operation of the imager is duly acknowledged. S. Chakrabarti and R. Rathi acknowledge the partial support from the above-mentioned grant. S. Chakrabarti acknowledges the fellowship from the Digital Futures Mobility Program (Project no. 8317), KTH, Stockholm, Sweden. J. Upadhyaya acknowledges the fellowship from the University Grant Commission, Government of India. R. Rathi acknowledges the fellowship from NERC grant NE/W003090/1, Physics Department, Lancaster University, United Kingdom. D. Patgiri acknowledges the fellowship from the Ministry of Education, Government of India, for carrying out this research work. The work is also supported by the Ministry of Education, Government of India.

Appendix A

Framework1: Deep Learning based Image Segmentation

Step1: Algorithm for Pixel Thresholding for Generation of Mask

---

```
# Function responsible for histogram stretch
func_histogram_stretch (image, new_min, new_max):
hist,bins = create_histogram(image, bins=256, range = [0,256]
hist_norm = hist/sum(hist)
cum_dis_func = hist_norm.cumsum()
min_Val, max_Val, min_Loc, max_Loc = MinMaxLoc(image)
old_min = min_Val
old_max = max_Val
stretch_func = func{(x - old_min) * (new_max - new_min) / (old_max - old_min) + new_min}
stretched_image = stretch_func(image)
return (stretched_image)

# Function to map intensity level (Contrast stretch)
func_pixel_val (pix, r1, s1, r2, s2):
 if (0 <= pix and pix <= r1)
       return (s1 / r1)*pix
 elseif (r1 < pix and pix <= r2)
       return ((s2 - s1)/(r2 - r1)) * (pix - r1) + s1
  else
       return ((255 - s2)/(255 - r2)) * (pix - r2) + s2
Define parameters: r1,s1,r2,s2
pixelVal_vec = func_vectorize(pixel_val)

# Thresholding Function
func_apply_threshold (image, threshold):
thresholded_image = func_where(image >= threshold, 1, 0)
return (thresholded_image)
```

Step2(a): Working Principle of Hybrid Image Segmentation Model

---

The working principle for the VGG16-UNet hybrid model can be summarized as follows:

1. **Input Image (*Image_data*):** The input image of shape H×W×C, H is the height, W is the width and C is the number of channels.
2. **Encoder Feature Extraction:** The VGG16 model extracts features from different layers:
   $F_1, F_2, \ldots, F_n = VGG16(Image\_data)$
3. **Decoder (Up-sampling):** The decoder up samples the feature maps while using skip connections:
   $D_1 = Up\ (F_n)$
   $D_2 = Conv(Concat(D_1, F_{n-1}))$
   Continues for all layers until the original image size is restored.
4. **Segmentation Output:** The output layer generates the segmented image:

Output = Softmax/Sigmoid (Conv1x1(D_n))

Step2(b): Algorithm for Hybrid Image Segmentation Model

#Initialization of VGG16 Model (Encoder)
Load pre-trained VGG-16 model (without fully connected layer) as Encoder
m_VGG16 = VGG16(include_top = False, weights = ‘imagenet’, input_shape =(input_shape))
set_trainable = ‘**False**’
for layer in VGG16.layers
    if layer_name in ['block1_conv1']:
        set_trainable = ‘**True**’
    if layer_name in ['block1_pool','block2_pool','block3_pool','block4_pool','block5_pool']
        layer_trainable = **‘False’**

#Extraction of Features using VGG16
Block1_c1 = VGG16.get_layer("block1_conv2").output
Block2_c2 = VGG16.get_layer("block2_conv2").output
Block3_c3 = VGG16.get_layer("block3_conv3").output
Block4_c4 = VGG16.get_layer("block4_conv3").output
Block5_c5 = VGG16.get_layer("block5_conv3").output

#Decoder (Up-sampling) using U-Net Model
m_up1 = Conv2DTranspose(size, last_layer)
m_up1 = func_activation(learning_rate, m_up1)
concat_1 = func_concatenate(m_up1, Block4_c4)
Continue Up-sampling and concatenation for successive blocks

#Final Output Layer and Compilation
model = func_model(inputs = inputs, outputs = outputs)
model_compile= func_model(optimizer = optimizer(learning_rate), loss_func, metrics)

#Training, Evaluation and Image Segmentation
final_model = train_model(image, threshold_image)
prediction_seg = final_model.predict(test_image

Appendix B

Framework2: Automatic Estimation of Propagation Parameters (Velocity & Orientation)

Algorithm:

```
#Loading segmentation model and Input file
seg_output = []
Model_seg = load (final_model)
for images in Event folder
    Input_file = load (Event folder)
    seg_output [] = seg_output.append(Model_seg.predict(Input_file))
end for

# Locating the plasma structure and condition to skip frames
for i in range length(seg_output) #Selecting frames
     Img = seg_output[i]
     x_min = [] #Column Numbers
     y_min = [] #Row Numbers
     for j in range (0, size(Img)) #Scanning each row of the image for minima
        Min_1 = Img.location[j].min()
        y_min.append(j) #y coordinate of minima
        x_min = x_min.append(Img.location[m].index_min()) #x coordinate of minima
    end for
     slope1, intercept1 = func_best_fit(x_min, y_min, 1) #Finding the first best fit line
     x_best_fit1 = x_min
     y_best_fit1= slope1*x_min + intercept1

     Squared error has been used to remove far away points and a second set of coordinates
     (best_x and best_y) are obtained to find the second-best fit line

     slope2, intercept2 = func_best_fit(best_x, best_y, 1) #Finding the second best fit line
     x_best_fit2 = best_x
     y_best_fit2= slope2* best_x + intercept2

     slope2 has been appended in slope_best_fit for all the frames

    for k in range length(best_x) #Condition to skip frames
        Finding the distance of the minima points from the second-best fit line
        Finding the average of the distances (Avg_dist)
        count = 0
        for l in range length(best_x)
            if dist(minima point) < Avg_dist
              count = count + 1
            end if
```

```
                if count > 75% of length(best_x)
                  skip = 0
                else
                  skip = 1
               end if
          end for
       end for
   end for
   Finding time difference (dt) of the selected frames (skip or no skip) after the skip condition

   # Determination of propagation parameters and error calculation
   Find the mid-point of each best fit line (x_Mid, y_Mid)
   Find the slope and intercept of the perpendicular lines from the mid points
   slope_perp = -1/slope2
   intercept_perp = (y_Mid – slope_perp*x_Mid)
   Find the intersection points of perpendicular lines & the successive best fit line (x_Int, y_Int)

   # Loading zonal and meridional distance files
   f = Read_file(Event_h5_file)
   meridional_dis = func_extract(f [‘Gridded Meridional Distance’])
   zonal_dis = func_extract(f ['Gridded Zonal Distance'])

  final_vel = []
  final_vel_error = []
  for m in range length(seg_output)-1 # Velocity calculation
      med_dis1= meridional_dis[y_Int]
      zon_dis1= zonal_dis[x_Int]
      med_dis2 = meridional_dis[y_Mid]
      zon_dis2 = zonal_dis[x_Mid]
      vel_zon = (zon_dis2 – zon_dis1)/dt[m] # Zonal velocity
      vel_med = (med_dis2 - med_dis1)/dt[m] # Meridional velocity
      distance = func_sqroot(sqr(med_dis2 - med_dis1) + sqr(zon_dis2 – zon_dis1))
      vel = distance[m]/dt[m] # Horizontal velocity
      final_vel.append(vel)

      std_err_pixel = func_std_error(scattered_points) # Velocity error calculation
      std_err_dis = (std_err_pixel)*(per_pixel_dis)
      vel_error = (std_err_dis[m] + std_err_dis[m+1]) /dt[m]
      final_vel_error.append(vel_error)
   end for

  tilt_angle = []
  final_tilt_angle_error = []
  for n in range length(slope_best_fit) # To calculate the tilt angle
```

```
        slope = slope_best_fit[n]
        angle_radian = func_inverse_tan(slope)
        angle_degree = (angle_radian*180)/func_pi
        angle_degree = (90 – angle_degree) + angle_of_declination (1.56) # Tilt angle
        prop_angle = angle_degree + 90 # Propagation direction
        tilt_angle.append(angle_degree)

        # To calculate the error of angle
       Intersecting line joining (x_Mid, y_Mid) and (x,y)
      slope_inter = (y – y_Mid)/(x – x_Mid)
      angle_err_radian = func_inverse_tan((slope_inter – slope2)/(1+slope2*slope_inter))
      angle_err_degree = (angle_err_radian*180)/func_pi
      final_tilt_angle_error.append(angle_err_degree)
  end for
```

References

Ayeni, J., 2022. Convolutional neural network (CNN): the architecture and applications. Appl. J. Phys. Sci., 4(4), pp.42-50. http://dx.doi.org/10.31248/AJPS2022.085

Bakki, P., 2002. On the region of mid-latitude spread-F. Acta Geod. et Geophys. Hung., 37(4), pp.409-417. https://doi.org/10.1556/ageod.37.2002.4.4.

Bovik, A.C., 2009. Basic binary image processing. In The Essential Guide to Image Processing (pp. 69-96). Academic Press. https://doi.org/10.1016/B978-0-12-374457-9.00004-4

Bowman, G.G., 1981. The nature of ionospheric spread-F irregularities in mid-latitude regions. J. Atmos. Solar-Terrestrial Phys., 43(1), pp.65-79. https://doi.org/10.1016/0021-9169(81)90010-6.

Chakrabarti, S., Patgiri, D., Rathi, R., Dixit, G., Krishna, M.S. and Sarkhel, S., 2024a. Optimizing a deep learning framework for accurate detection of the Earth's ionospheric plasma structures from all-sky airglow images. Adv. Sp. Res., 73(12), pp.5990-6005. https://doi.org/10.1016/j.asr.2024.03.014

[dataset] Chakrabarti, S., Patgiri, D., Rathi, R., Dixit, G., Krishna, M.S. and Sarkhel, S., 2024b. Optimizing a deep learning framework for accurate detection of the Earth's ionospheric plasma structures from all-sky airglow images. Zenodo Data, v1. https://doi.org/10.5281/zenodo.14222287

Ding, F., Wan, W., Xu, G., Yu, T., Yang, G. and Wang, J.S., 2011. Climatology of medium-scale traveling ionospheric disturbances observed by a GPS network in central China. J. Geophys. Res. Space, 116(A9). https://doi.org/10.1029/2011ja016545.

Fabel, Y., Nouri, B., Wilbert, S., Blum, N., Triebel, R., Hasenbalg, M., Kuhn, P., Zarzalejo, L.F. and Pitz-Paal, R., 2022. Applying self-supervised learning for semantic cloud segmentation of all-sky images. Atmospheric Measurement Techniques, 15(3), pp.797-809. https://doi.org/10.5194/amt-15-797-2022

Figueiredo, C.A.O.B., Takahashi, H., Wrasse, C.M., Otsuka, Y., Shiokawa, K. and Barros, D., 2018. Investigation of nighttime MSTIDS observed by optical thermosphere imagers at low latitudes: Morphology, propagation direction, and wind filtering. J. Geophys. Res. Space, 123(9), pp.7843-7857. https://doi.org/10.1029/2018ja025438.

Fukao, S., Kelley, M.C., Shirakawa, T., Takami, T., Yamamoto, M., Tsuda, T. and Kato, S., 1991. Turbulent upwelling of the mid-latitude ionosphere: 1. Observational results by the MU radar. J. Geophys. Res. Space, 96(A3), pp.3725-3746. https://doi.org/10.1029/90ja02253.

Fukao, S., McClure, J.P., Ito, A., Sato, T., Kimura, I., Tsuda, T. and Kato, S., 1988. First VHF radar observation of midlatitude F-region field-aligned irregularities. Geophys. Res. Lett., 15(8), pp.768-771. https://doi.org/10.1029/GL015i008p00768

Gao, X., Fu, R., Li, X., Tao, D., Zhang, B. and Yang, H., 2011. Aurora image segmentation by combining patch and texture thresholding. Comput. Vis. Image Underst., 115(3), pp.390-402. https://doi.org/10.1016/j.cviu.2010.11.011

Githio, L., Liu, H., Arafa, A.A. and Mahrous, A., 2024. A machine learning approach for estimating the drift velocities of equatorial plasma bubbles based on All-Sky Imager and GNSS observations. Adv. Sp. Res., 74(11), pp.6047-6064. https://doi.org/10.1016/j.asr.2024.08.067

Hasenbalg, M., Kuhn, P., Wilbert, S., Nouri, B. and Kazantzidis, A., 2020. Benchmarking of six cloud segmentation algorithms for ground-based all-sky imagers. Sol. Energy., 201, pp.596-614. https://doi.org/10.1016/j.solener.2020.02.042

Hocke, K. and Schlegel, K., 1996, September. A review of atmospheric gravity waves and travelling ionospheric disturbances: 1982–1995. In Ann. Geophys. (Vol. 14, No. 9, p. 917). https://doi.org/10.1007/s005850050357.

Huang, F., Dou, X., Lei, J., Lin, J., Ding, F. and Zhong, J., 2016. Statistical analysis of nighttime medium-scale traveling ionospheric disturbances using airglow images and GPS observations over central China. J. Geophys. Res. Space, 121(9), pp.8887-8899. https://doi.org/10.1002/2016ja022760.

Huang, F., Lei, J., Dou, X., Luan, X. and Zhong, J., 2018. Nighttime medium-scale traveling ionospheric disturbances from airglow imager and Global Navigation Satellite Systems observations. Geophys. Res. Lett., 45(1), pp.31-38. https://doi.org/10.1002/2017gl076408.

Ioffe, S., 2015. Batch normalization: Accelerating deep network training by reducing internal covariate shift. arXiv preprint arXiv:1502.03167. https://proceedings.mlr.press/v37/ioffe15.html.

Kumar, L., Sahay, S.K. and Kusneniwar, H.G., 2023. An investigation of two-step cascaded CNN for the detection of gravitational wave signal from two different astronomical sources. Procedia Comput. Sci., 222, pp.676-684. https://doi.org/10.1016/j.procs.2023.08.205

Lai, C., Xu, J., Lin, Z., Wu, K., Zhang, D., Li, Q., Sun, L., Yuan, W. and Zhu, Y., 2023. Statistical characteristics of nighttime medium-scale traveling ionospheric disturbances from 10-years of airglow observation by the machine learning method. Sp. Weather, 21(5), p.e2023SW003430. https://doi.org/10.1029/2023SW003430

Lai, C., Xu, J., Yue, J., Yuan, W., Liu, X., Li, W. and Li, Q., 2019. Automatic extraction of gravity waves from all-sky airglow image based on machine learning. Remote Sens., 11(13), p.1516. https://doi.org/10.3390/rs11131516

Liu, P., Yokoyama, T., Fu, W., and Yamamoto, M., 2022. Statistical analysis of medium-scale traveling ionospheric disturbances over Japan based on deep learning instance segmentation. Sp. Weather, 20, e2022SW003151. https://doi.org/10.1029/2022SW003151

Mathews, J.D., Gonzalez, S., Sulzer, M.P., Zhou, Q.H., Urbina, J., Kudeki, E. and Franke, S., 2001. Kilometer-scale layered structures inside spread-F. Geophys. Res. Lett., 28(22), pp.4167-4170. https://doi.org/10.1029/2001gl013077.

Miller, C.A., 1997. Electrodynamics of midlatitude spread F. 2. A new theory of gravity wave electric fields: Aeronomy of the solstice thermosphere/ionosphere system. Part 2. J. of geophys. res., 102(A6), pp.11533-11538. https://doi.org/10.1029/96JA03840.

Mondal, S., Srivastava, A., Yadav, V., Sarkhel, S., Krishna, M.S., Rao, Y.K. and Singh, V., 2019. Allsky airglow imaging observations from Hanle, Leh Ladakh, India: Image analyses and first results. Adv. Sp. Res., 64(10), pp.1926-1939. https://doi.org/10.1016/j.asr.2019.05.047.

Niu, C., Zhang, J., Wang, Q. and Liang, J., 2018. Weakly supervised semantic segmentation for joint key local structure localization and classification of aurora image. IEEE Transactions on Geosci. and Remot. Sens., 56(12), pp.7133-7146. https://doi.org/10.1109/TGRS.2018.2848725

Otsuka, Y., Shiokawa, K., Ogawa, T. and Wilkinson, P., 2004. Geomagnetic conjugate observations of medium-scale traveling ionospheric disturbances at midlatitude using all-sky airglow imagers. Geophys. Res. Lett., 31(15). https://doi.org/10.1029/2004gl020262.

Otsuka, Y., Shiokawa, K. and Ogawa, T., 2012. Disappearance of equatorial plasma bubble after interaction with mid-latitude medium-scale traveling ionospheric disturbance. Geophys. Res. Lett., 39(14). https://doi.org/10.1029/2012gl052286.

Otsuka, Y., Tani, T., Tsugawa, T., Ogawa, T. and Saito, A., 2008. Statistical study of relationship between medium-scale traveling ionospheric disturbance and sporadic E layer activities in summer night over Japan. J. Atmos. Solar-Terrestrial Phys., 70(17), pp.2196-2202. https://doi.org/10.1016/j.jastp.2008.07.008.

Patgiri, D., Rathi, R., Yadav, V., Sarkhel, S., Chakrabarty, D., Mondal, S., Krishna, M.S., Upadhayaya, A.K., Vivek, C.G., Kannaujiya, S. and Sunda, S., 2024a. A case study on multiple self-interactions of MSTID bands: New insights. Adv. Sp. Res., 73(7), pp.3595-3612. https://doi.org/10.1016/j.asr.2023.05.047

Patgiri, D., Rathi, R., Yadav, V., Chakrabarty, D., Sunil Krishna, M.V., Kannaujiya, S., Pavan Chaitanya, P., Patra, A.K., Liu, J.Y. and Sarkhel, S., 2024b. A rare simultaneous detection of a mid-latitude plasma depleted structure in O (1D) 630.0 and O (1S) 557.7 nm all-sky airglow images on a geomagnetically quiet night. Geophys. Res. Lett., 51(14), p.e2023GL106900. https://doi.org/10.1029/2023GL106900

Paulino, I., Moraes, J.F., Maranhão, G.L., Wrasse, C.M., Buriti, R.A., Medeiros, A.F., Paulino, A.R., Takahashi, H., Makela, J.J., Meriwether, J.W. and Campos, J.A.V., 2018, February. Intrinsic parameters of periodic waves observed in the OI6300 airglow layer over the Brazilian equatorial region. In Ann. Geophys. (Vol. 36, No. 1, pp. 265-273). Göttingen, Germany: Copernicus Publications. https://doi.org/10.5194/angeo-36-265-2018. https://doi.org/10.5194/angeo-36-265-2018.

Pimenta, A.A., Amorim, D.C.M. and Candido, C.M.N., 2008. Thermospheric dark band structures at low latitudes in the Southern Hemisphere under different solar activity conditions: A study using OI 630 nm emission all-sky images. Geophys. Res. Lett., 35(16). https://doi.org/10.1029/2008gl034904.

Rathi, R., Gurram, P., Mondal, S., Yadav, V., Sarkhel, S., Krishna, M.S. and Upadhayaya, A.K., 2024. Unusual simultaneous manifestation of three non-interacting mid-latitude ionospheric plasma structures. Adv. Sp. Res., 73(7), pp.3550-3562. https://doi.org/10.1016/j.asr.2023.04.038

Rathi, R., Yadav, V., Mondal, S., Sarkhel, S., Krishna, M.S. and Upadhayaya, A.K., 2021. Evidence for simultaneous occurrence of periodic and single dark band MSTIDs over geomagnetic low-mid latitude transition region. J. Atmos. Solar-Terrestrial Phys., 215, p.105588. https://doi.org/ 10.1016/j.jastp.2021.105588.

Rathi, R., Yadav, V., Mondal, S., Sarkhel, S., Sunil Krishna, M.V., Upadhayaya, A.K., Kannaujiya, S. and Chauhan, P., 2022. A Case Study on the Interaction Between MSTIDs' Fronts, Their Dissipation, and a Curious Case of MSTID's Rotation Over Geomagnetic Low-Mid Latitude Transition Region. J. Geophys. Res. Space, 127(4), p.e2021JA029872. https://doi.org/10.1029/2021JA029872

Ronneberger, O., Fischer, P. and Brox, T., 2015. U-net: Convolutional networks for biomedical image segmentation. In Medical image computing and computer-assisted intervention–MICCAI 2015: 18th international conference, Munich, Germany, October 5-9, 2015, proceedings, part III 18 (pp. 234-241). Springer Int. Pub. https://doi.org/10.48550/arXiv.1505.04597

Shelhamer, E., Long, J., and Darrell, T. 2017. Fully Convolutional Networks for Semantic Segmentation. IEEE Trans. Pattern Anal. Mach. Intell., 39(4), p.640-651. https://doi.org/10.1109/TPAMI.2016.2572683

Shiokawa, K., Ihara, C., Otsuka, Y. and Ogawa, T., 2003. Statistical study of nighttime medium-scale traveling ionospheric disturbances using midlatitude airglow images. J. Geophys. Res. Space, 108(A1). https://doi.org/10.1029/2002ja009491.

Shiokawa, K., Otsuka, Y., Tsugawa, T., Ogawa, T., Saito, A., Ohshima, K., Kubota, M., Maruyama, T., Nakamura, T., Yamamoto, M. and Wilkinson, P., 2005. Geomagnetic conjugate observation of nighttime medium-scale and large-scale traveling ionospheric disturbances: FRONT3 campaign. J. Geophys. Res. Space, 110(A5). https://doi.org/10.1029/2004ja010845.

Simonyan, K. and Zisserman, A., 2014. Very deep convolutional networks for large-scale image recognition. arXiv preprint arXiv:1409.1556. https://doi.org/10.48550/arXiv.1409.1556

Sivakandan, M., Mondal, S., Sarkhel, S., Chakrabarty, D., Sunil Krishna, M.V., Chaitanya, P.P., Patra, A.K., Choudhary, R.K., Pant, T.K., Upadhayaya, A.K. and Sori, T., 2020. Mid-latitude spread-F structures over the geomagnetic low-mid latitude transition region: An observational evidence. J. Geophys. Res. Space, 125(5), p.e2019JA027531. https://doi.org/10.1029/2019JA027531.

Sivakandan, M., Mondal, S., Sarkhel, S., Chakrabarty, D., Sunil Krishna, M.V., Upadhayaya, A.K., Shinbori, A., Sori, T., Kannaujiya, S. and Champati Ray, P.K., 2021. Evidence for the In-Situ Generation of Plasma Depletion Structures Over the Transition Region of Geomagnetic Low-Mid Latitude. J. Geophys. Res. Space, 126(9), p.e2020JA028837. https://doi.org/10.1029/2020JA028837.

Sun, L., Xu, J., Wang, W., Yue, X., Yuan, W., Ning, B., Zhang, D. and De Meneses, F.C., 2015. Mesoscale field-aligned irregularity structures (FAIs) of airglow associated with medium-scale traveling ionospheric disturbances (MSTIDs). J. Geophys. Res. Space, 120(11), pp.9839-9858. https://doi.org/10.1002/2014ja020944.

Takeo, D., Shiokawa, K., Fujinami, H., Otsuka, Y., Matsuda, T.S., Ejiri, M.K., Nakamura, T. and Yamamoto, M., 2017. Sixteen year variation of horizontal phase velocity and propagation direction of mesospheric and thermospheric waves in airglow images at Shigaraki, Japan. J. Geophys. Res. Space, 122(8), pp.8770-8780. https://doi.org/10.1002/2017JA023919

Tsuboi, T., Shiokawa, K., Otsuka, Y., Fujinami, H. and Nakamura, T., 2023. Statistical Analysis of the Horizontal Phase Velocity Distribution of Atmospheric Gravity Waves and Medium-Scale Traveling Ionospheric Disturbances in Airglow Images Over Sata (31.0° N, 130.7° E), Japan. J. Geophys. Res. Space, 128(12), p.e2023JA031600. https://doi.org/10.1029/2023JA031600

Wang, H., Cao, P., Wang, J. and Zaiane, O.R., 2022, June. Uctransnet: rethinking the skip connections in u-net from a channel-wise perspective with transformer. In Proceedings of the AAAI conference on artificial intelligence (Vol. 36, No. 3, pp. 2441-2449).

Wu, K., Xu, J., Wang, W., Sun, L. and Yuan, W., 2021. Interaction of oppositely traveling medium-scale traveling ionospheric disturbances observed in low latitudes during geomagnetically quiet nighttime. J. Geophys. Res. Space, 126(2), p.e2020JA028723. https://doi.org/10.1029/2020JA028723.

Xie, W., Liu, D., Yang, M., Chen, S., Wang, B., Wang, Z., Xia, Y., Liu, Y., Wang, Y. and Zhang, C., 2020. SegCloud: A novel cloud image segmentation model using a deep convolutional neural network for ground-based all-sky-view camera observation. Atmos. Meas. Tech., 13(4), pp.1953-1961. https://doi.org/10.5194/amt-13-1953-2020

Yadav, V., Rathi, R., Gaur, G., Sarkhel, S., Chakrabarty, D., Krishna, M.S., Chaitanya, P.P., Patra, A.K., Choudhary, R.K., Pant, T.K. and Upadhayaya, A.K., 2021a. Interaction between nighttime MSTID and mid-latitude field-aligned plasma depletion structure over the transition region of geomagnetic low-mid latitude: First results from Hanle, India. J. Atmos. Solar-Terrestrial Phys., 217, p.105589. https://doi.org/10.1016/j.jastp.2021.105589.

Yadav, V., Rathi, R., Sarkhel, S., Chakrabarty, D., Sunil Krishna, M.V. and Upadhayaya, A.K., 2021b. A unique case of complex interaction between MSTIDs and mid-latitude field-aligned plasma depletions over geomagnetic low-mid latitude transition region. J. Geophys. Res. Space, 126(1), p.e2020JA028620. https://doi.org/10.1029/2020JA028620

Zhang, J., Liu, P., Zhang, F. and Song, Q., 2018. CloudNet: Ground-based cloud classification with deep convolutional neural network. Geophys. Res. Lett., 45(16), pp.8665-8672. https://doi.org/10.1029/2018GL077787

Figures:

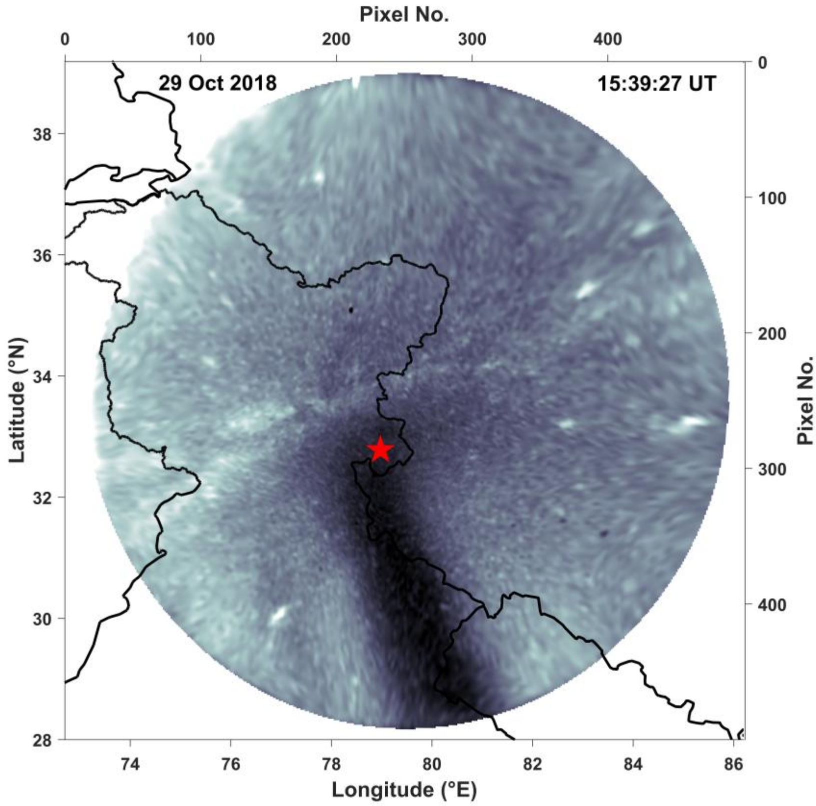

Figure 1: Example of an airglow image with latitude-longitude range and pixel number. The red star denotes the location of the airglow imager at Hanle, Ladakh, India.

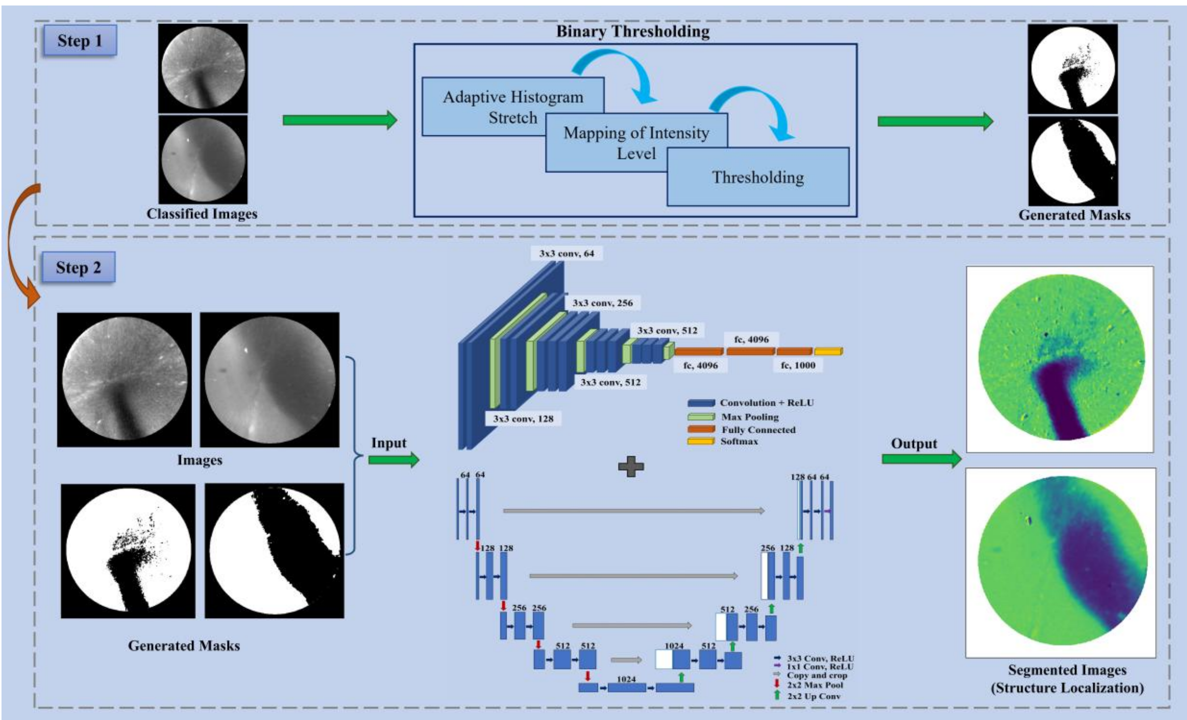

Figure 2: Pictographic representation of Framework 1.

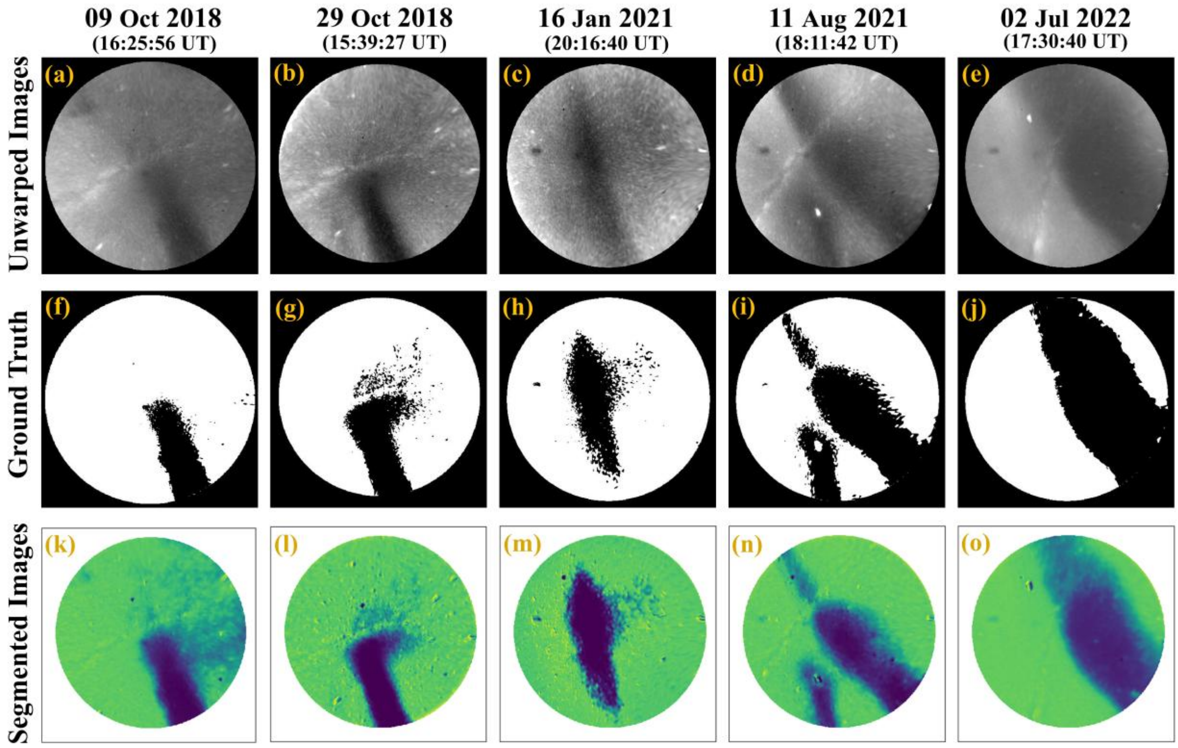

Figure 3: Five instances of unwarped images (top row) with corresponding ground truth (middle row) and the segmented images (bottom row) from the hybrid model.

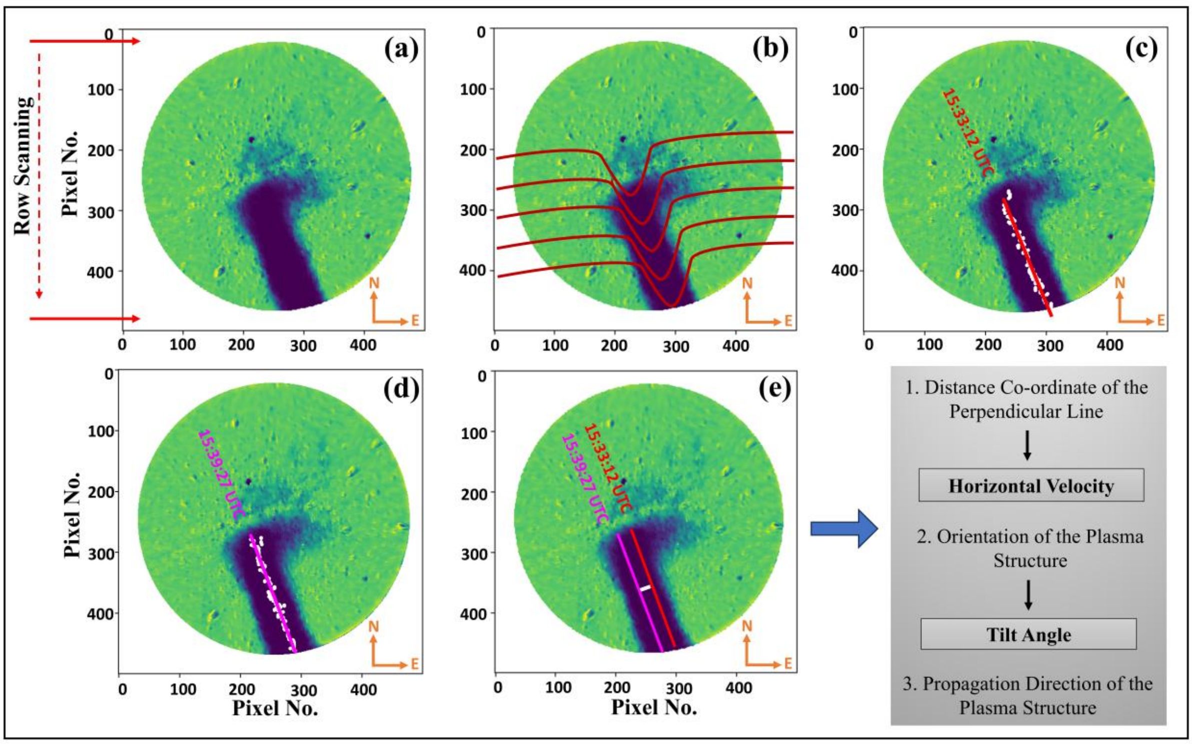

Figure 4: Illustration of steps in Framework 2 for estimation of propagation parameters.

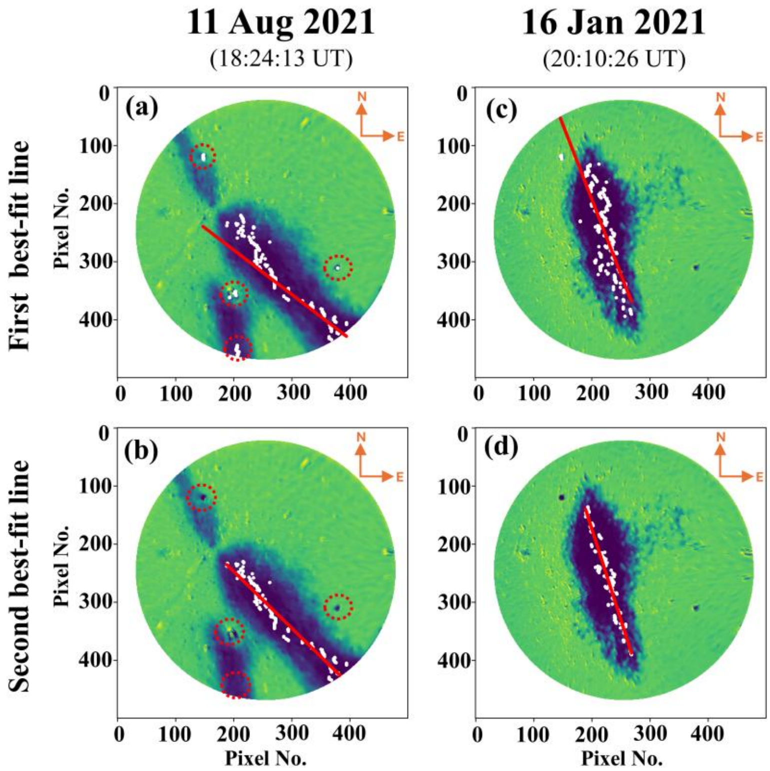

Figure 5: Two examples showing the difference between the first and the second best-fit line.

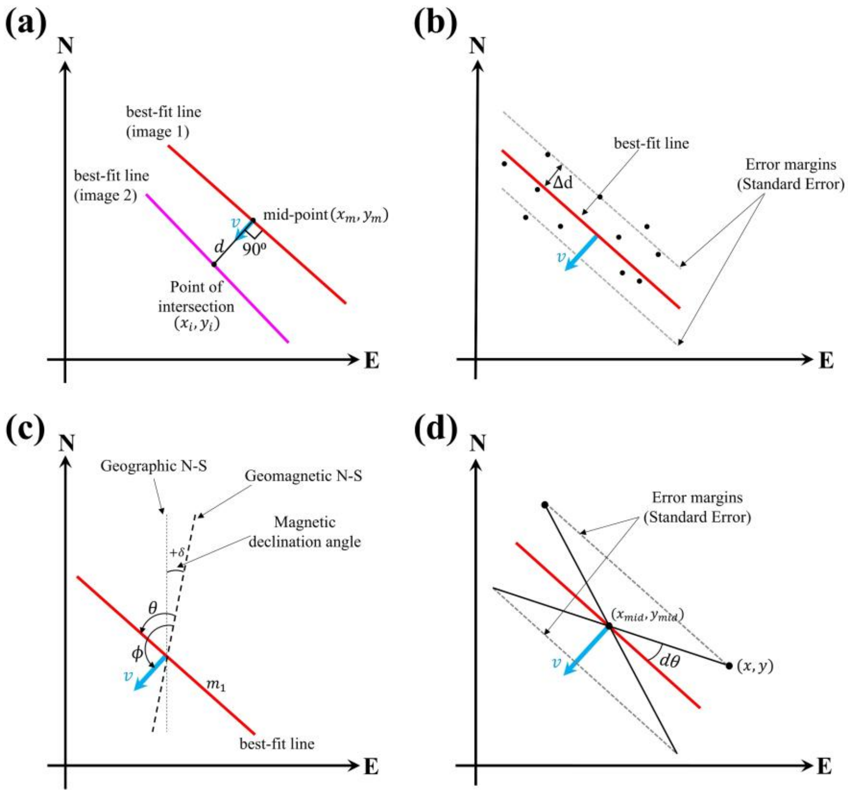

Figure 6: Schematic representation of the methods used for calculation of propagation parameters and the error involved with it.

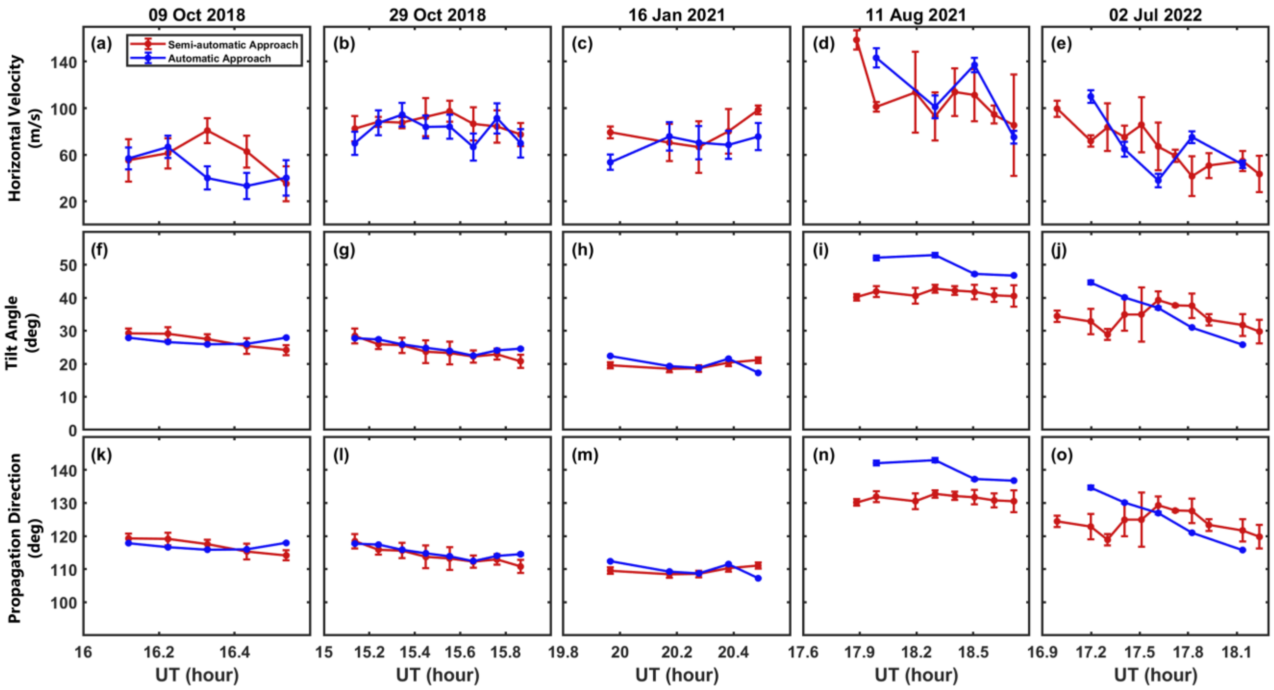

Figure 7: The calculated horizontal velocity, tilt angle, and propagation direction using semi-automatic (red) and automatic (blue) approaches with their estimated errors.

Tables:

Table 1: Average horizontal, zonal and meridional velocity with the estimated errors using both automatic and semi-automatic method

Date	Skip	Time (UT)	Average Horizontal Velocity ± Average Error (m/s)		Average Zonal Velocity ± Average Error (m/s)		Average Meridional Velocity ± Average Error (m/s)	
			Automatic	Semi-Automatic	Automatic	Semi-Automatic	Automatic	Semi-Automatic
09-10-2018	0	16:25:56 to 16:57:12	47.43 ± 11.11	59.00 ± 15.14	-43.25 ± 10.02	-52.66 ± 13.67	-19.39 ± 4.80	-26.51 ± 6.83
29-10-2018	0	15:08:11 to 15:58:12	80.93 ± 9.83	87.00 ± 10.44	-73.98 ± 10.04	-79.87 ± 9.95	-32.59 ± 4.31	-34.29 ± 4.63
16-01-2021	0	19:57:56 to 20:35:26	68.76 ± 11.29	78.97 ± 13.26	-65.89 ± 10.72	-75.20 ± 12.77	-19.45 ± 3.53	-24.04 ± 4.08
11-08-2021	1	17:52:58 to 18:49:13	114.11 ± 7.38	108.90± 20.21	-83.87 ± 4.94	-83.76 ± 15.78	-77.13 ± 5.46	-69.54 ± 12.97
02-07-2022	1	16:59:25 to 18:20:40	67.91 ± 5.17	66.58 ± 13.00	-58.81 ± 4.28	-55.75 ± 11.17	-33.47 ± 2.85	-36.10 ± 7.28

Table 2: Average tilt angle and propagation direction (anti-clockwise from geomagnetic N-S) with the estimated errors using both automatic and semi-automatic method

Date	Skip	Time (UT)	Average Tilt Angle (θ) ± Average Error (deg)		Propagation Direction(ϕ) ± Average Error (deg)	
			Automatic	Semi-Automatic	Automatic	Semi-automatic
09-10-2018	0	16:25:56 to 16:57:12	27.22 ± 0.15	27.09 ± 1.85	117.23 ± 0.15	117.07 ± 1.85
29-10-2018	0	15:08:11 to 15:58:12	24.95 ± 0.11	24.09 ± 2.29	114.95 ± 0.12	114.09 ± 2.29
16-01-2021	0	19:57:56 to 20:35:26	19.76 ± 0.11	19.58 ± 1.00	109.77 ± 0.11	109.58 ± 1.00
11-08-2021	1	17:52:58 to 18:49:13	48.58 ± 0.40	41.31 ± 1.88	138.58 ± 0.40	131.31 ± 1.88
02-07-2022	1	16:59:25 to 18:20:40	34.93 ± 0.26	34.12 ± 3.25	124.93 ± 0.26	124.12 ± 3.25